

Azimuth Antenna Maximum Likelihood Estimation by Persistent Point Scatterers in SAR images

Pietro Guccione, Andrea Monti Guarnieri, *Member, IEEE*, and Mariantonietta Zonno

I. INTRODUCTION

THE persistent scatterers (PS) technique [1] is a powerful and fully operational tool for monitoring ground deformations by exploiting long time series of synthetic aperture radar (SAR) images taken with similar geometry. PS techniques have found application for accurate monitoring of relative displacements, in the interpretation of the PS physical nature [2], for accurate DEM generation [3], in the study of millimeter slow deformation in urban areas such as those associated with underground excavations, water extraction, and subsidence in mining areas, [4], [5], to perform cross-interferogram and get very long coherent time series to determine with extreme accuracy the location of targets [6], and so on.

The main feature of a persistent scatterer is that it keeps a high stability of its amplitude and phase over the time series, so that the atmospheric phase screen, the line-of-sight displacement of topography, and the velocity of deformation changes can be estimated by proper unwrapping of the PS grid on the image. The stability is usually accounted for as the ratio between the mean amplitude over the series and its standard deviation. This index is commonly called the dispersion index [7].

Manuscript received June 29, 2012; revised December 12, 2012; accepted February 3, 2013. Date of publication March 22, 2013; date of current version December 12, 2013. This work was supported by the framework of Italian Space Agency (ASI) AO-1080, under the conditions as in ASI document DC-OST-2009-116.

P. Guccione and M. Zonno are with the Dipartimento di Elettrotecnica ed Elettronica, Politecnico di Bari, Bari 70125, Italy (e-mail: pietro.guccione@gmail.com; m.zonno@poliba.it).

A. Monti Guarnieri is with the Dipartimento di Elettronica e Informazione, Politecnico di Milano, Milano 20132, Italy (e-mail: monti@elet.polimi.it).

Color versions of one or more of the figures in this paper are available online.

Most recently, PS has been used for the calibration of SAR images [7], [8]. The idea is to exploit a suitable set of targets over many images instead of proper test sites that include transponders, which is known to be a more expensive solution. The targets must be stable in amplitude and phase; coherent detection is applied to perform an optimal estimation of the image amplitude, target amplitude, level of clutter, and target phase. The analysis of the targets that show such requirements reveals that PS can often be considered satisfactory point targets for which amplitude stability implies phase stability and vice versa and for which this stability is assured for a long time, at least as long as the available temporal baseline. However, this is not always true; stable targets coming from bare rock dihedrals, for example, do not show impulsive trend characteristics.

We propose here to explicitly restrict the study of PS to the class of point PS (PPS). In fact, the physical nature of the target has been already investigated in previous works [2], [9], but PPS have not been yet exploited for their impulsive trend features. These targets can be selected by quantifying their similarity with respect to an ideal point target. The method, partly investigated in [10] and [11], is presented here in more detail and justified using new data. The relation between a target's impulsive behavior in azimuth and in slant range is a function of the target's physical nature and orientation. In [2], six typologies of targets are classified on the basis of their physical size, number of wave bounces, and radar cross section, and it is found that for specific targets (isotropic), as pole or trihedral, the impulsive trend in both the directions are correlated. However, to the aim of azimuth antenna pattern estimation, just the azimuth impulsive trend requirement will be investigated. PPS are expected to be less numerous than the traditional PS as to the classical amplitude stability (i.e., high dispersion index). Further, an impulsive trend is required, as well as sufficient isolation from other strong scatterers nearby. The last requirement guarantees no relevant effects of aliasing on the azimuth spectrum of the target when focused by means of the digital spotlight technique [12], [13].

The rest of this paper is organized as follows. In Section II, the theoretical model of PPS is outlined. In Section III, the azimuth antenna pattern estimation method is described. Experimental evidences to support the PPS model and some results of the estimation are provided in Section IV. Finally, conclusions are given in Section VI.

II. DATA MODEL

The standard model for the statistics of the complex signal backscattered by a ground area illuminated by a single-look SAR sensor adopts the circular Gaussian, zero-mean, and equal variance joint statistics for real and imaginary parts [14]. Unfortunately, that model is no longer valid in contexts such as urban areas and high-resolution SAR images [9], [15], [16].

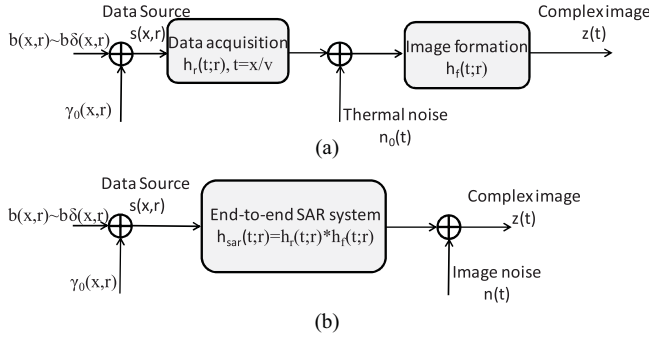


Fig. 1. Continuous-time SAR system. (a) Acquisition and image formation processes. (b) Equivalent end-to-end system (the image gain a is not represented in the figure).

A possible simplified model for such a case is

$$s(x, r) = \gamma^0(x, r) + b(x - x_0, r - r_0) \quad (1)$$

where γ^0 is the complex reflectivity of a distributed and homogeneous scatterer, modeled as a realization of a complex spatially uncorrelated zero-mean Gaussian process and $b(x - x_0, r - r_0)$ is a target superimposed on the distributed scatterer and located at (x_0, r_0) in the (x, r) data plane. In a first approximation the target is deemed point-like: $\simeq b \cdot \delta(x - x_0, r - r_0)$ (this assumption is relaxed in Section III). The source data is hence regarded as the coherent superposition of a strong and dominant reflector plus weaker and homogeneous entities.

Fig. 1 illustrates a simplified formulation of the SAR acquisition and focusing processes. In the following analysis we assume that processing can be limited to the one-dimensional case, even though the proper range variant kernel is assumed whenever azimuth focusing is referred to. The blocks in the upper part of Fig. 1 are hence regarded as linear time-invariant filters; the received thermal noise that adds to the raw data, $n^0(t)$, is deemed as a white, zero-mean Gaussian process. The simplified model for the acquisition system impulse response h_r is then [17]

$$h_r(t; r) \propto A_{az} \left(\frac{v}{r} (t - t_{dc}) \right) \cdot \exp(j\pi f_R t^2) \quad (2)$$

where $\psi_{dc} = vt_{dc}/r$ is the squint angle due to the centroid, r is the target slant range, v is the sensor speed, f_R is the Doppler rate, and $A_{az}(t; r)$ is the azimuth antenna pattern that, in a first approximation, follows the sinc² shape.

The focusing (or image formation) is the process that regresses raw data back to an estimate of the complex reflectivity. The commonly used approach is to build a phase-matched filtering $h_f(t; r)$ with $\angle h_f(t; r) = \exp(-j\pi f_R t^2)$. The cascade of the acquisition and focusing represents the end-to-end SAR system (represented in the lower part of Fig. 1). For a given target, the end-to-end response $z(t)$ is then (the dependence on distance r is no longer represented)

$$\begin{aligned} z(t) &= a [h_{sar}(t) * s(t) + h_f(t) * n^0(t)] \\ &= a [h_{sar}(t) * b(t) + n(t)] \end{aligned} \quad (3)$$

where

$$\begin{cases} h_{sar}(t) = h_r(t) * h_f(t), \\ n(t) = h_{sar}(t) * \gamma^0(t) + h_f(t) * n^0(t) \end{cases} \quad (4)$$

and a the acquisition and processing gain. In $n(t)$, the additive image noise and the distributed homogeneous target have been included, as both are Gaussian zero-mean processes, even

though no longer white, according to the bandwidth of the acquisition and focusing operators.

The azimuth spectrum of such data is the Fourier transform \mathcal{F} of (3)

$$Z(f) = a \cdot [H_{sar}(f) \cdot b(f) + N(f)] \quad (5)$$

with $H_{sar}(f) = \mathcal{F}\{h_{sar}(t)\}$ and $|H_{sar}| = A_{az}(f - f_{dc})$ for the phase-matched filtering. The antenna shape in the time domain is a function of the sensor-target angle-of-view $\psi = vt/r$, which, under the narrow-band hypothesis, is proportional to the Doppler frequency f : $\psi \simeq -\lambda/2v \cdot f$. So the acquisition and processing transfer functions have the same amplitude shape. The spectrum amplitude $b(f)$, is the Fourier transform of the point target. Under ideal conditions (i.e., isotropic target and very high SNR), $b(f)$ should be a constant.

To effectively describe the SAR system, azimuth sampling should be accounted for. Aliasing occurs due to the periodic repetition of the transfer function as well as of the source data

$$Z(f) = a \left[\sum_n b(f - n \cdot PRF) \cdot H_{sar}(f - n \cdot PRF) + W(f) \right] \quad (6)$$

having renamed $Z(f)$ the periodic version of the data spectrum first term of (5) and with $W(f)$ the periodic version of $N(f)$. However, the effect of aliasing is different for a point target and for a distributed scatterer. For a point target, the spectral replica is separated in the frequency domain by PRF and, for the time/frequency relation, by a time interval ΔT

$$\begin{aligned} f &= -\frac{2v}{\lambda} \sin \psi = -\frac{2v}{\lambda} \sin \left(\frac{vt}{R} \right) \rightarrow, \\ \Delta T_n &= \frac{R}{v} \arcsin \left(-\frac{\lambda}{2v} n \cdot PRF \right) \simeq -\frac{\lambda R}{2v^2} n \cdot PRF \end{aligned} \quad (7)$$

which can be accounted for by processing the azimuth strip using a spotlight kernel [12], [13], [18]. On the other side, the terms of a distributed scatterer cannot be separated, as contributions at different frequencies (that are uncorrelated) add up. For the distributed scatterer, we have

$$E[\Gamma(f)] = \sum_n E[\Gamma^0(f - n \cdot PRF)] \cdot H_{sar}(f - n \cdot PRF) = 0 \quad (8)$$

$$\begin{aligned} E[\Gamma(f)\Gamma^*(f)] &= \sum_n \sum_m E[\Gamma^0(f - n \cdot PRF)\Gamma^{0*}(f - m \cdot PRF)] \\ &\quad \times H_{sar}(f - n \cdot PRF)H_{sar}^*(f - m \cdot PRF) \\ &= \sigma_s^2 \sum_n |H_{sar}(f - n \cdot PRF)|^2 \end{aligned} \quad (9)$$

where $\Gamma^0(f) = \mathcal{F}\{\gamma^0(t)\}$ and $\sigma_s^2 = E[|\gamma^0|^2]$. Since $\Gamma^0(f)$ is Gaussian distributed, i.e., $\Gamma^0(f) \sim \mathcal{N}(0, \sigma_s^2)$, the discrete-time model for the distributed scatterer is an uncorrelated and zero-mean process input to

$$H(f) = \sum_n H_{sar}(f - n \cdot PRF).$$

Similar result is achieved for the image noise.

In conclusion, spotlight processing differently affects point targets and distributed scatterers. Ambiguities can be isolated and removed for a single point target, as they are spatially separated by time intervals ΔT , while this is not the case for a distributed scatterer for which the contributions add up. In a real image, both point targets and distributed scatterers are present and the effect of spotlight processing is to combine

them, generating noise ambiguity on strong point targets, which finally impacts the antenna estimation accuracy. More insight is provided in Section IV-B.

III. AZIMUTH ANTENNA PATTERN ESTIMATION

A. Multitarget Problem Formulation

The accurate knowledge and monitoring of the azimuth antenna pattern (AAP) is of fundamental importance for the calibration of modern SAR systems, which was traditionally devoted to transponders or corner reflectors [19]. Here, the AAP amplitude is frequency-wise estimated (as in [20]), together with other parameters, by the maximization of the likelihood of the joint statistics of a set of stable and impulsive targets. A quantitative measure of the targets' impulsive trend is adopted to select the subset of targets exploited for the estimate. Details on such measure and on targets selection algorithm are provided in Sections III-B and III-C, respectively.

Let us assume to have identified a set of P stable targets on a stack of N interferometric images for which

$$Z(f) = a[b(f)H(f) + W(f)] \quad (10)$$

holds derived from (6) after considerations on sampling and super-resolution processing. Since SAR data are bandpass in azimuth, with maximum of the band centered around the Doppler centroid, (10) is reformulated using zero-centered azimuth spectra, which follows after estimation of the centroid [21]–[23]. The multitarget formulation considers a spectrum folding of period $Q \cdot PRF$, as targets are supposed to be focused at super-resolution with Q the oversampling factor

$$Z_{n,p}(f) = a_n A_{ant}(f) |b_p(f)| \exp(j\phi_{n,p}(f)) + a_n W_p(f) \quad (11)$$

where (n, p) are the image-target indexes, $A_{ant}(f)$ is the amplitude of the (folded) SAR transfer function $|H(f)|$, and $\phi_{n,p}(f) = \angle\{H(f)b_p(f)\}$ is the spectrum phase, i.e., the Fourier transform of the focused target phase that accounts for the contribution proper of each target (the intrinsic target phase) and the overall target-to-sensor two way optical path, which is affected by contributions from the DEM, the target deformation over time, and the APS [7], [24].

The previous formulation implies that a single antenna model can be inferred by varying the set of targets and the stack of images. In fact, for practical systems, the antenna active elements excitation coefficients are very different for different acquisitions, depending on the scene condition and mission planning program. The antenna pattern is then expected to be different for different images, $A_{ant}(f) = A_n(f)$. A more precise formulation is then

$$\begin{aligned} Z_{n,p}(f_m) &= a_n A_n(f_m) b_p(f_m) \exp(j\phi_{n,p}(f_m)) + a_n W_p(f_m) \\ \rightarrow Z_{m,n,p} &= a_n A_{m,n} b_{m,p} \Phi_{m,n,p} + a_n W_{m,p} \end{aligned} \quad (12)$$

having accounted for the discretization of the frequency axis within the azimuth non-ambiguous interval $m \in [-Q \cdot PRF/2, Q \cdot PRF/2]$, $m = 1, \dots, M$, with $b_p(f_m) = |b_p(f_m)|$ and $\Phi_{m,n,p} = \exp(j\phi_{n,p}(f_m))$.

The products in the second term of (12), i.e., $X_{m,n,p} = a_n A_{m,n} b_{m,p} \Phi_{m,n,p}$, and $V_{m,n,p} = a_n W_{m,p}$ can be compactly written in vector notation as

$$\mathbf{Z} = \mathbf{X} + \mathbf{V} \quad (13)$$

with \mathbf{Z} , \mathbf{X} , and \mathbf{V} column vectors of size $[MNP, 1]$, and

$$\begin{cases} \mathbf{X} = [(\mathbf{a}\mathbf{1}_P^T)_v \mathbf{1}_M^T] \otimes [(\mathbf{A}\mathbf{1}_P^T)_v] \otimes [(\mathbf{b}\mathbf{1}_N^T)_v] \otimes \Phi \\ \mathbf{V} = [(\mathbf{a}\mathbf{1}_P^T)_v \mathbf{1}_M^T] \otimes [(\mathbf{b}\mathbf{1}_N^T)_v] \end{cases} \quad (14)$$

with

$$\begin{cases} \mathbf{a} = [a_1, \dots, a_N]^T \\ \mathbf{b} = [b_{1,1}, b_{1,2}, \dots, b_{M,P}]^T \\ \mathbf{A} = [A_{1,1}, A_{1,2}, \dots, A_{MN}]^T \\ \Phi = [\Phi_{1,1,1}, \Phi_{1,1,2}, \dots, \Phi_{M,N,P}]^T \\ \mathbf{1}_L^T = [1, 1, \dots, 1], \quad \text{of size } [1 \times L] \end{cases}$$

where \otimes is the Hadamard product and $(Q)_v$ denotes the column vector achieved by concatenating the rows of the matrix Q .

The noise \mathbf{V} is circular complex zero-mean normally distributed

$$f(\mathbf{V}) \sim \mathcal{N}(0, \mathbf{C}_v) = \frac{\exp(-\mathbf{V}^* \mathbf{C}_v^{-1} \mathbf{V})}{\pi^{MNP} |\mathbf{C}_v|} \quad (15)$$

with a diagonal covariance matrix, assuming a white noise power spectral density i.e. large and flat bandwidth of the focusing operator in (3)

$$\mathbf{C}_v = [\text{diag}[(\mathbf{a}\mathbf{1}_P^T)_v \mathbf{1}_M^T]] \otimes [\text{diag}[(\Sigma^2 \mathbf{1}_N^T)_v]] \quad (16)$$

with $\Sigma^2 = [\sigma_{1,1}^2, \sigma_{1,2}^2, \dots, \sigma_{M,P}^2]$ the noise variances in the spectrum domain, associated to the P targets and M frequencies and due to the image noise and distributed scatterer contributions. The log-likelihood of the joint statistics in (15) is

$$\mathcal{L}(\mathbf{Z}|\mathbf{X}, \mathbf{C}_v) = -(\mathbf{Z} - \mathbf{X})^* \mathbf{C}_v^{-1} (\mathbf{Z} - \mathbf{X}) - \log |\mathbf{C}_v| \quad (17)$$

which, after some maths (see Appendix) gives

$$\begin{aligned} \mathcal{L}(\mathbf{Z}|\mathbf{a}, \mathbf{A}, \mathbf{b}, \Sigma^2) &= - \sum_{m,n,p} \frac{|Z_{m,n,p}|^2}{a_n^2 \sigma_{m,p}^2} - N \sum_{m,n,p} \frac{A_{m,n}^2 b_{m,p}^2}{\sigma_{m,p}^2} \\ &+ 2\Re \left\{ \sum_{m,n,p} \frac{Z_{m,n,p}^* A_{m,n} b_{m,p} \Phi_{m,n,p}}{a_n \sigma_{m,p}^2} \right\} \\ &- MP \sum_n \log a_n^2 - N \sum_{m,p} \log \sigma_{m,p}^2 \end{aligned} \quad (18)$$

where \Re is the real part and, without loss of generality, the gain of the first image has been set to 1, as absolute gains cannot be known without an external reference. In (18), the unknowns \mathbf{a} , \mathbf{b} , \mathbf{A} , and Σ^2 can be estimated thanks to the observations \mathbf{Z} and the hypothesis of normal joint distribution for \mathbf{V} [8], [25]. Equation (18) is a nonlinear expression in the unknowns that can be solved iteratively, starting from an approximate solution [7]. Details are in the Appendix.

B. Target Selection Strategy

In principle, the formulation in (18) can be solved for any set of targets modeled as in Section II, but Φ must be added to the other unknowns in this case. In practice, a more rapid convergence of the iteration procedure is reached if targets are really impulsive and a good SNR is supposed, so that the effect of target spectral shape and noise becomes negligible and amplitude of observations resembles the antenna pattern. Another reason to select just the “best” (and then few) targets for the implementation of (18) is that observations \mathbf{Z} are focused in super-resolution (to catch the antenna sidelobes) and this is a computationally demanding task.

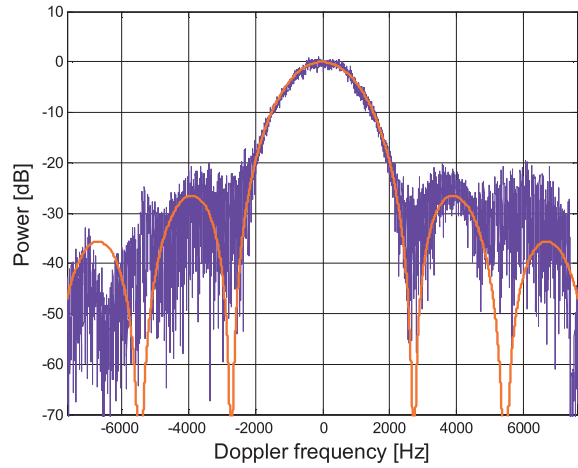


Fig. 2. Power spectral density of an impulsive trend target ($I_{n,p} = 6.95$) with SNR = 25.3 dB, focused at super-resolution ($5 \times \text{PRF}$). The target has been taken from a Cosmo SkyMed image. Superimposed, in red, is the ideal antenna pattern power spectrum (i.e., $\text{sinc}^4(\frac{L_{ant}}{2b} f)$, L_{ant} is the antenna length).

Let us reformulate (18) including the previous hypotheses, i.e., targets are impulsive and with a sufficiently high SNR. Under these conditions, it is reasonable to put

$$\mathcal{L}Z_{n,p}(f) \simeq \Phi_{n,p}(f)$$

which allows us to simplify (18) in

$$\begin{aligned} \mathcal{L}(\mathbf{Z}|\mathbf{a}, \mathbf{A}, \mathbf{b}, \Sigma^2) = & - \sum_{m,n,p} \frac{1}{\sigma_{m,p}^2} \left[\frac{|Z_{m,n,p}|}{a_n} - A_{m,n} b_{m,p} \right]^2 \\ & - MP \sum_n \log a_n^2 - N \sum_{m,p} \log \sigma_{m,p}^2. \end{aligned} \quad (19)$$

For the best targets, the maximization of \mathcal{L} with respect to antenna implies the minimization of the first contribution on the right-hand side of (19), which easily leads to

$$|Z_{m,n,p}| \simeq a_n b_{m,p} A_{m,n}. \quad (20)$$

In a first approximation, the spectral shape can be estimated frequency-wise by the ratio $|Z_{n,p}(f)|/a_n A_n(f)$, provided that antenna and image gains have been otherwise estimated.

For this reason, the following index:

$$I_{n,p} = \sqrt{\int [|Z_{n,p,dB}(f)| - a_{n,dB} A_{id,dB}(f)]^2 df} \quad (21)$$

integrated over the nonambiguous interval $f \in [-Q \cdot \text{PRF}/2, Q \cdot \text{PRF}/2]$, with A_{id} the ideal (and folded) version of the antenna represents a compact measure of how much a target owns an impulsive trend. It is called the similarity index and basically is the root-mean-square error (RMSE) of the difference between the two spectra (properly normalized) measured in dB, to better account for large amplitude variations. The lower the value of $I_{n,p}$, the closer the target under examination to an ideal point.

A visual illustration of such similarity between the power spectral density of a high-SNR target taken from a Cosmo SkyMed image and the ideal antenna is shown in Fig. 2. The spectrum amplitude, even though noisy, resembles the azimuth antenna pattern up to the second sidelobe. However, the frequency/angular shape depends also on the target radiation

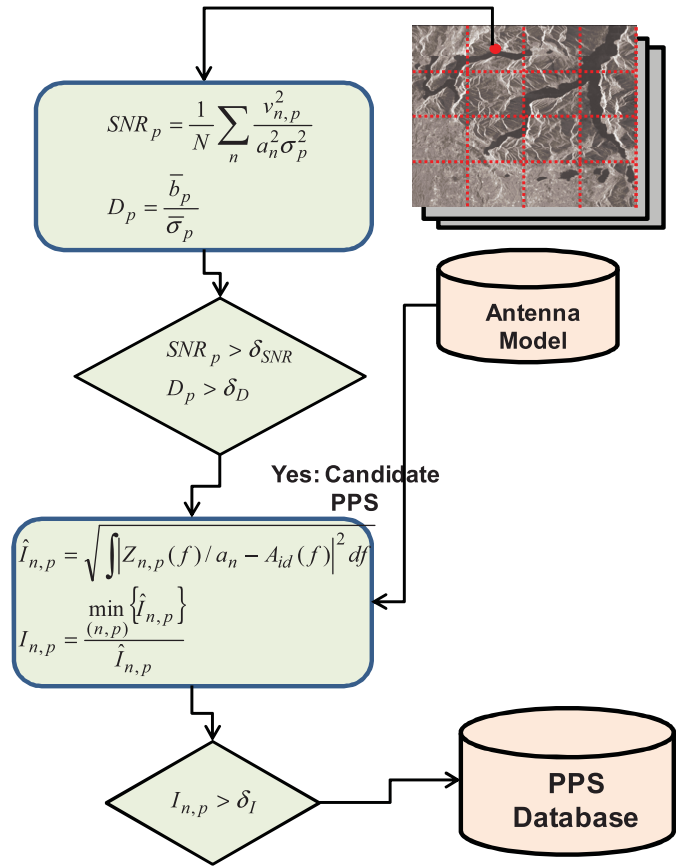


Fig. 3. Block diagram of the PPS selection algorithm.

pattern, which can be solved only by processing multiple images and considering stable targets.

Proper thresholds to the SNR, dispersion index, and similarity index allow us to select a suitable set of targets for antenna estimation, sparing computational time and reaching at the same time a good accuracy of the result. Empirical distributions of such measures were used to select the thresholds. Further details are in Section IV.

C. PPS Selection Algorithm

Selection of PPS from a stack of interferometric SAR images is a screening process, which, starting from a set of PS, takes the potential PPS discarding the unfit ones by using a threshold on the similarity index. In the following, a description of the PPS selection algorithm (illustrated in Fig. 3) is provided. In principle, retrieving a set of PS is not a part of the PPS selection algorithm; however, for a given stack of interferometric images it is not expected that location, SNR, and dispersion index of a set of PS are given. For this reason, the algorithm consists basically of two steps: 1) a set of persistent scatterers are identified in the stack of images and 2) the similarity index is computed for the target and a threshold is used to select a restricted subset.

PS selection was performed by following the simple method originally proposed in [1], for which a target stable in amplitude (high dispersion index) is a good PS candidate. Since we are interested in targets that are both stable and possess sufficiently high SNR (this restriction avoids getting hundreds of thousands or millions of targets coming from usual PS

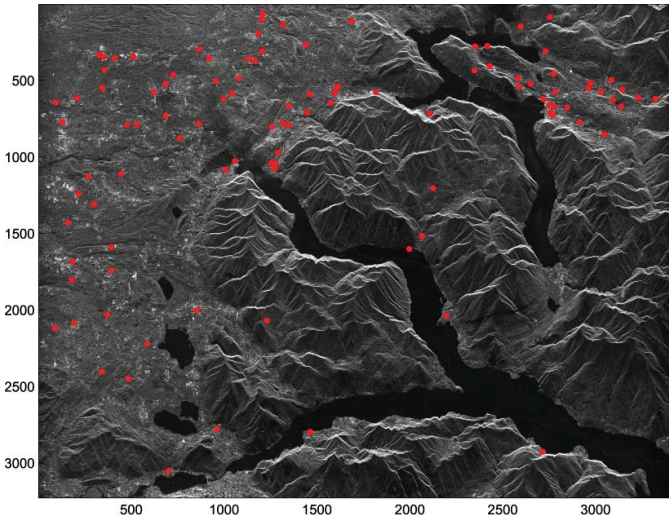


Fig. 4. Multilook image of the lakes area north of Milan, Italy, and, in red, the PPS selected for the antenna estimation (see Table II). The dataset was acquired on September 3, 2008, at 05:16:06 h. The image resolution is about 30 m. Azimuth is the horizontal axis, slant range the vertical axis.

detection), a threshold on the target SNR was imposed. Given \bar{b}_p and $\bar{\sigma}_p$ the mean and the standard deviation of the amplitudes for the p -th target throughout the images in the stack, the dispersion index is defined as

$$D_p = \frac{\bar{b}_p}{\bar{\sigma}_p}. \quad (22)$$

Targets selected as PS are those satisfying both the following conditions:

$$\begin{aligned} \text{SNR}_p &> \delta_{\text{SNR}} \\ D_p = \frac{\bar{b}_p}{\bar{\sigma}_p} &> \delta_D. \end{aligned} \quad (23)$$

Selection of the optimal thresholds is discussed in Section IV-B.

For the set of PS, the similarity index $I_{n,p}$ was computed by means of (21) and then averaged over the images. In principle, all the targets screened by (23), more or less, could be considered PPS, apart for the possible presence of “false alarm” targets. For AAP estimation, the targets with a similarity index under a given threshold are retained as PPS

$$I_p < \delta_I. \quad (24)$$

It turned out very convenient to fix δ_I as a percentile: for the AAP estimation, δ_I establishes what percentage of the PS targets are effectively exploited to estimate the antenna. Note that, if the averaging of $I_{n,p}$ is not performed over the images, each single target in each image could be retained or not as PPS, according to δ_I . Of course, it is expected that PS targets possess a stable spectral shape that is hence always below or above the threshold, for a long temporal baseline.

IV. EXPERIMENTAL RESULTS

A. Experimental Dataset and Target Statistics

The PPS selection algorithm has been applied on a stack of 25 interferometric images acquired by the Cosmo SkyMed (CSK) constellation [26] during a time interval that covers over 3 years. Images were acquired by Cosmo 1 (14 images), Cosmo 2 (6), Cosmo 3 (3), and Cosmo 4 (2). The area selected

TABLE I
PPS SCREENING INPUT PARAMETERS AND RESULTS. THE SIMILARITY INDEX IS NORMALIZED AS IN (25)

Feature	Value
Number of images	25
Average sizes of the common area [ground rg × az]	40.4 × 43.9 km
Initial screening	
Threshold on SNR	$\delta_{\text{SNR}} = 5$ dB
Threshold on D	$\delta_D = 0.3$
Number of PS found	454434
Average number of PS/km ²	~ 256.2
Further screening	
Threshold on SNR	$\delta_{\text{SNR}} = 5$ dB
Threshold on D	$\delta_D = 2.5$
Restricted set of PS found	2496
Average SNR	18.19 dB
Average D	3.6463
Average similarity index	0.4345

for the analysis includes over 1700 km² on the great and medium lakes area north of Milan, Italy. In Fig. 4, a sketch of the area with the location of a set of PPS is provided.

In a first screening, a set of targets were found by using $\delta_{\text{SNR}} = 5$ dB and $\delta_D = 0.3$ (see Table I). As expected, this way a very large number of PS were selected. To avoid the computational overload coming from the super-resolution processing needed to compute (21), the similarity index has been determined just after a further screening, achieved by tightening the SNR with $\delta_{\text{SNR}} = 5$ dB and $\delta_D = 2.5$.

In Table I, the similarity index was normalized, to make it easier to compare the statistics coming from different datasets. The definition in (21) is then replaced by its inverse

$$\hat{I}_{n,p} = \frac{\min_{(n,p)} \{I_{n,p}\}}{I_{n,p}} \quad (25)$$

in order to have values always in the interval $[\eta, 1]$, arbitrarily assigning 1 to the best target in the set and $\eta = \min_{(n,p)} \{I_{n,p}\} / \max_{(n,p)} \{I_{n,p}\}$ to the worst target.

As outlined in Section II, non-Gaussian models are the most suited to represent point target features. Many of such models have been investigated, all providing some physical or experimental justification to explain the data distribution. The most commonly adopted models for the intensity are the Nakagami, Gamma, Fisher, Weibull, \mathcal{K} -root, or log-normal [16]. Different methods of PDF parameter estimation exist, the main being the maximum likelihood (ML), the method of moments (MoM), and the method of log-cumulants (MoLC) estimators. Weibull, log-normal, generalized Gamma (GF), and Fisher PDF models were tested on the empirical distribution of the targets amplitude, SNR dispersion index, and similarity index as in (25). By taking advantage of the results in [9] and [15], the MoLC was adopted for parameter estimation.

Results in Fig. 5 show that the log-normal distribution seems the most valuable to fit the experimental curves, and it is the one reported superimposed to the empirical curves.

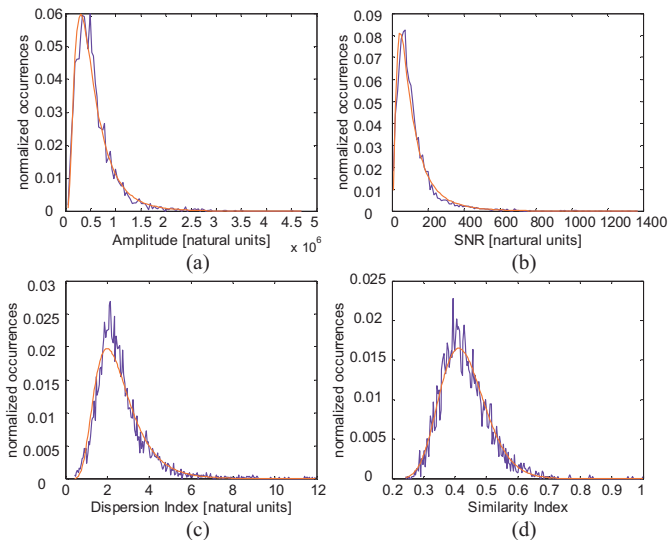


Fig. 5. Empirical distributions (in blue) and, superimposed, the log-normal estimated PDF model (red). (a) Amplitude, (b) SNR (in natural units), and (c) dispersion index reported for targets described in the second section of Table I. (d) Similarity index normalized as in (25) reported for the 2496 targets in Table I.

B. Target Density and Ambiguity Assessment

The candidates for antenna estimation are point targets processed by spotlight focusing, which is known to produce aliasing. Aliased data impact on the azimuth antenna estimation, as each target processed by spotlight processing is affected by ambiguity due to both distributed scatterers and point targets. The distributed scatterers are uncorrelated with the target, and the coherent summation gives an effect similar to thermal noise. The ambiguities generated by point target, on the other hand, are frequency correlated, but this case of aliasing is very infrequent. The limitations on the density of point target calibrators in a stack of images suitable for antenna estimation are hence addressed by the level of signal-to-noise ambiguity ratio (SNAR).

Provided that amplitudes are governed by a lognormal distribution (see Section IV-A and Fig. 5)

$$f(x) = \frac{1}{x\sqrt{2\pi\sigma^2}} e^{-\frac{(\log x - \mu)^2}{2\sigma^2}} \quad (26)$$

with a cumulative distribution function

$$F(x) = \frac{1}{2} + \frac{1}{2} \operatorname{erf} \left(\frac{\log x - \mu}{\sqrt{2}\sigma} \right) \quad (27)$$

the probability that a target, after attenuation by antenna pattern (about 26 dB), still keeps a good SNR, say 10 dB, is

$$\xi = 10^{-\frac{36}{20}}$$

$$F(\xi) = \frac{1}{2} + \frac{1}{2} \operatorname{erf} \left(\frac{\log \xi}{\sqrt{2}} \right) = 1.70 \times 10^{-5}$$

setting $\mu = 0$ and $\sigma = 1$. For an image of 3000×3000 pixels (see Fig. 4) we expect about $1.70 \times 10^{-5} \times 3000^2 = 153$ targets, which is comparable with the 128 calibrators used in Section IV-C for antenna pattern estimation.

Target SNAR affects the correct detection of targets and false alarm probability, according to the number of images and the level of threshold used for the dispersion index.

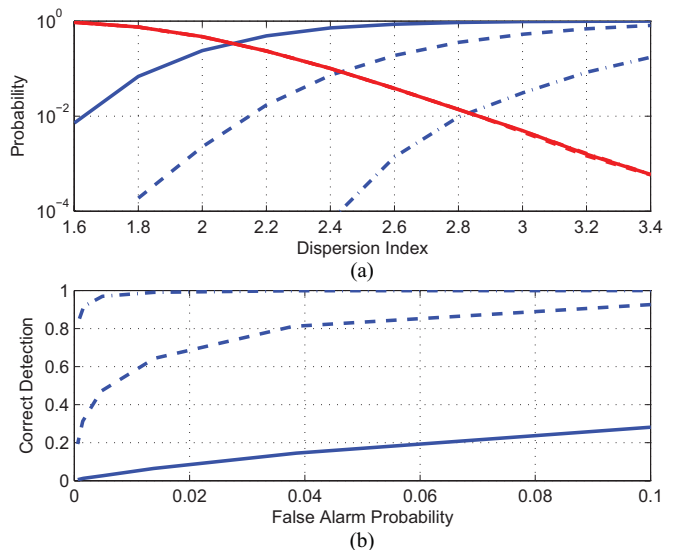


Fig. 6. (a) False alarm (red) and missing detection (blue) probabilities as a function of the dispersion index threshold for $L = 25$ images. (b) Correct detection probability as function of the false alarm for $L = 25$ images. Solid line: SNR = 0 dB, dotted line 5 dB, dotted-solid line: 10 dB.

TABLE II
PPS RESTRICTED SET FOR THE AAP ESTIMATION. THE SIMILARITY INDEX IS NORMALIZED AS IN (25)

Feature	Value
Initial set of PPS	2496
Threshold on similarity index	$\delta_I = 0.60$
Survived PPS	128 targets
Average SNR	16.61 dB
Average D	3.268
Average similarity index	0.657

In [7], the probabilities of false alarm and missed detection as a function of the threshold on the dispersion index and number of images were evaluated. It was shown that for 10 images and an SNR of 8 dB, both false alarm and missing detection were below 0.1 using a threshold on the dispersion index of 3. We repeated such simulations for different levels of images, SNR, and threshold of dispersion index, finding that in the case of $L = 25$ (the ones available for this study) and using a dispersion index of 2.5, a relatively low level of false alarm (less than 10%) with a good level of correct detection (over 99%) for targets with SNR = 10 dB are reached (see in Fig. 6). Little differences were found for a number of images in the interval $20 \div 35$.

C. Antenna Estimation Results

The azimuth antenna pattern was estimated with a subset of 128 targets. The targets were selected on the basis of their high similarity index, i.e., the most delta-like targets were chosen. The empirical distribution of the similarity index was used to set such threshold, finding 128 targets with $\delta_I > 0.60$. A summary of the selected targets is given in Table II.

For comparison, a set of simulated point targets were generated by using the same mean and dispersion for the SNR, and the same number of images and targets. Simulated point targets were not generated as perfect impulses: a low-pass

TABLE III
SIMULATION PARAMETERS FOR THE SET OF PPS

Parameter	Value
Number of targets	128
Number of images	25
Simulated apertures	5
Kind of spectral shape	Polynomial second-order window
Spectral shape -3 dB width	$2 \times \text{PRF}$
Std. of the spectral shape width	$0.75 \times \text{PRF}$
Amplitude random variation model	Gaussian PDF
Std. of ampl. variation between datasets (w.r.t. a ref. level)	20%
Doppler centroid random variation model	Gaussian PDF
Std. of Doppler centroid variation	20 Hz
Mean SNR	16.6 dB
Simulated PDF for the SNR	Gaussian
Standard deviation of SNR	2.0 dB

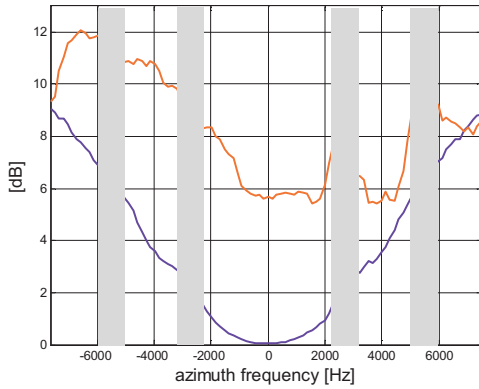


Fig. 7. Standard deviation of the target spectral shape estimates as a function of the frequency. Red curve: CSK data. Blue curve: simulated set. The frequency intervals experiencing antenna nulls have been masked by gray bars.

second-order window was applied as spectral signature, the width of the window (so the degree of low-passing effect) being randomly variable. Targets' spectra were finally shifted by a random value to simulate the presence of a residual, not estimated, Doppler centroid. The system and geometrical parameters for the simulation were those of the Cosmo SkyMed constellation [26], whose main parameters are collected in Table III.

The dispersion (computed as standard deviation) of the target spectral shape estimates as a function of the frequency is plotted in Fig. 7. This large dispersion was an expected result, as each shape refers to a single target, i.e., an object of different physical nature and independent of the other targets. The average dispersions for the real and simulated datasets are comparable, providing 8.32 and 3.92 dB, respectively. The lower value for the simulated set can be explained by noticing that the simulation has not accounted for the secondary but not negligible effect of the different viewpoint of each acquisition which produces, for each target, a different cross-section and then a different spectral shape.

The single-images antenna estimates are illustrated in Fig. 8. The superposition of the estimates provides a graphic impression of the antenna shape dispersion for the

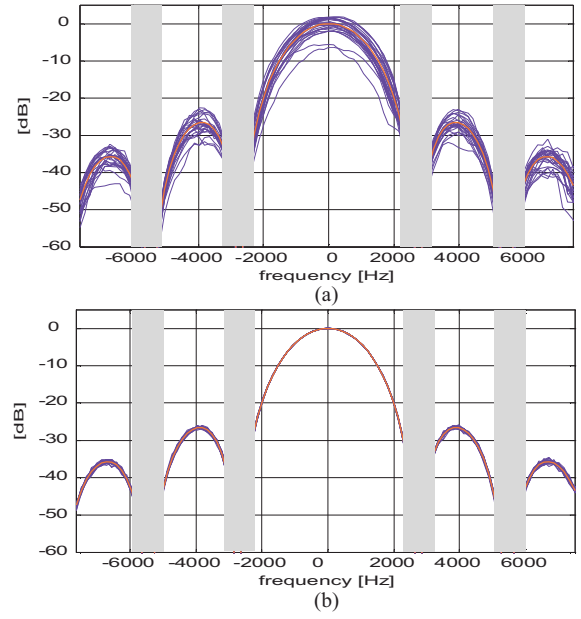


Fig. 8. The Azimuth antenna patterns estimated over the stack of images and, superimposed, the ideal antenna pattern. (a) Real dataset: RMSE = 2.37 dB. (b) Simulated dataset: RMSE = 0.38 dB.

four CSK sensors and during the 3 years of acquisition. The average dispersion is computed as

$$\text{RMSE} = \sqrt{\frac{\sum_{m=1}^M \sum_{n=1}^N |\hat{A}_{est,dB}^{(n)}(f_m) - \hat{A}_{est,dB}(f_m)|^2}{M \cdot N}} \quad (28)$$

where $\hat{A}^{(n)}$ is the antenna shape estimate for the n th image of the stack and \hat{A} is the average estimate. Estimated antennas have a stable behavior that well resembles the ideal pattern (sinc^2 shape, superimposed in red). A comparison with the set of simulated targets [see Fig. 8(b)] shows that the two results, which give a measure of the antenna pattern stability over the temporal baseline, are comparable, providing for the real CSK data an RMSE of 2.37 dB versus 0.38 dB of the simulated set (again, the difference can be due to the lacking of perfect simulation conditions).

An interesting measure is the distance between the antenna estimate and the ideal model (Fig. 9), as it quantifies the antenna pattern proximity to the ideal pattern and can be used to monitor the status of the antenna throughout the mission lifetime. As can be noted, the average difference throughout 3 years and for the 4 satellites is retained within 1 dB.

The detail of the distance of each antenna estimate with respect to the ideal antenna can be exploited to flag possible malfunctioning occurring during the acquisition. This distance is computed as

$$\text{RMSE}_n = \sqrt{\frac{\sum_{m=1}^M |\hat{A}_{est,dB}^{(n)}(f_m) - A_{id,dB}(f_m)|^2}{M}} \quad (29)$$

As can be noted, all the RMSE values are below 2.5 dB (see Fig. 10), except for three measures which provided higher values. Perhaps this behavior could be due to a bad programming of the antenna pattern acquisition, even though it seems more

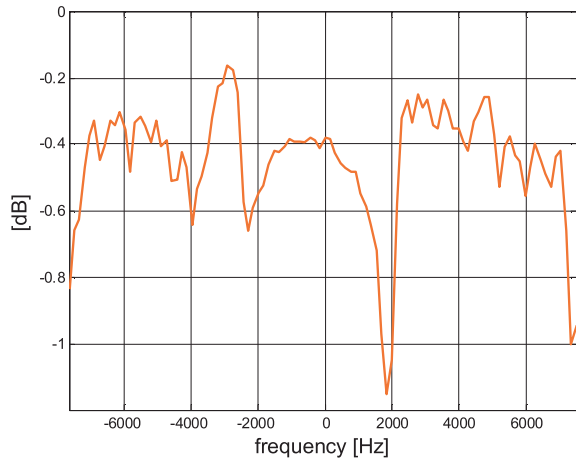


Fig. 9. Difference between the antenna pattern average estimate and the ideal model for the CSK datasets. The ideal antenna model is generated as a folded version of the $\text{sinc}^2(L_{\text{ant}}/2vf)$.

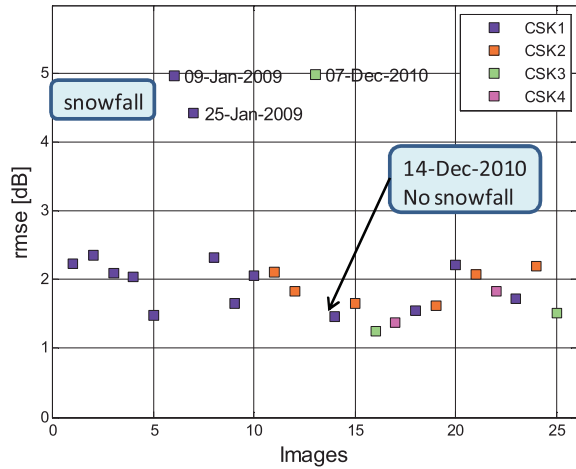


Fig. 10. RMSE between each single estimate and the ideal antenna model for the 25 CSK acquisitions.

plausible as due to a remarkable difference of the targets' nature just in those days. Even though the considerations on the possible hypotheses go beyond the purpose of this paper, we verified that on all the three dates a big snowfall occurred, while, for comparison, in the remaining winter date no precipitation happened, nor in a few days before.

V. CONCLUSION

In this paper, we presented the azimuth antenna pattern estimation by means of PPS. PPS was selected as a subset of the PS; super-resolution processing and isolation from neighboring scatterers were used to retrieve them from a set of PS. The antenna similarity index was finally used to choose the ones suitable for antenna pattern estimation.

The azimuth antenna pattern estimation was formulated by a joint statistical approach, and the maximum likelihood applied to retrieve also the targets' spectral shape and the image gains. A subset of PS was exploited for the estimation based on considerations of SNAR and the heavy computational time. The method was successfully applied on a set of Cosmo Sky Med datasets, acquired by the four satellites over a period of 3 years. The CSK antenna pattern was shown to be very

stable in this period and for the different satellites, providing an average distance with respect to the ideal antenna of about 1 dB.

PPS have been already used for accurate Doppler centroid estimation¹; future applications can include exact target positioning as well as accurate image registration. As further development, the study can be extended to the analysis of the relationship between targets physical nature, and statistical features, as well as to the PPS distribution over different types of areas such as urban, forest, and so on.

APPENDIX

Taking advantage of the noise uncorrelation and matrix algebra, (17) can be developed to achieve a simpler formulation

$$\begin{aligned} \mathbf{Z}^* \mathbf{C}_v^{-1} \mathbf{Z} &= \sum_m \sum_n \sum_p \frac{|Z_{m,n,p}|^2}{a_n^2 \sigma_{m,p}^2} \\ \mathbf{X}^* \mathbf{C}_v^{-1} \mathbf{X} &= \sum_m \sum_n \sum_p \frac{A_{m,n}^2 b_{m,p}^2}{\sigma_{m,p}^2} \\ 2\Re \{ \mathbf{Z}^* \mathbf{C}_v^{-1} \mathbf{X} \} &= 2\Re \left\{ \sum_m \sum_n \sum_p \frac{Z_{m,n,p}^* A_{m,n} b_{m,p} \Phi_{m,n,p}}{a_n \sigma_{m,p}^2} \right\} \\ \log |\mathbf{C}_v| &= N \sum_m \sum_p \log \sigma_{m,p}^2 + MP \sum_n \log a_n^2. \end{aligned} \quad (30)$$

The final expression for the log-likelihood \mathcal{L} can be achieved by applying two different approaches to the spectrum phase, i.e., by supposing it completely unknown: in this case we speak of incoherent estimation; the alternative is to suppose a structured model, typically a first (or second) order polynomial [7]: in this second case, a coherent estimation is applied.

Here the spectrum phase has been described by a second-order polynomial (structured model)

$$\phi_{n,p}(f_m) = \alpha_n f_m^2 + \beta_n f_m + \gamma + \epsilon_n(m, p) \quad (31)$$

where the set of image-dependent coefficients α , β , and γ can be achieved by applying a weighted least mean square procedure to the phase of observations before computing the log-likelihood. In detail, for each image the mean square of the error $\epsilon_n(m, p)$ between measures and model is minimized by varying the unknowns $\{\alpha_n, \beta_n, \gamma_n\}$

$$\{\alpha_n, \beta_n, \gamma_n\} = \min_{\{\alpha_n, \beta_n, \gamma_n\}} \left[\sum_p K_n(m) \epsilon_n(m, p)^2 \right]. \quad (32)$$

The formulation of (32) is more effective than an unweighted minimization, as it provides relative importance to the errors on the basis of the variance of the measures $Z(f)$ throughout the frequencies; this is justified by the fact that the measurements, even though uncorrelated, have different uncertainties at the different frequencies. The weights are chosen so that

$$K_n(f_m) \propto \frac{1}{\text{var}_p [Z_{n,p}(f_m)]}. \quad (33)$$

For the Gauss–Markov theorem, this method ensures to find the best linear unbiased estimator for the \mathcal{LZ} . We incidentally notice that, after the WLMS step, the set of α_n and β_n

¹A paper on this subject has been submitted to TGRS.

are proportional to the unestimated bias of the Doppler rate and Doppler centroid, respectively. After the estimation and correction of the $\angle Z$, it is obvious to suppose a completely random behavior for the residual phase of \mathbf{Z} ; for this reason, an incoherent approach is used to solve (17).

According to [7], the residual phase in (17) is then estimated by maximizing the log-likelihood with respect to the unknown phase (here not treated); then $\hat{\phi}_{m,n,p} = -\angle(Z_{n,p}(m))$ is replaced back into (17), finally providing the expression in (19).

The maximization of \mathcal{L} with respect to the unknowns \mathbf{a} , \mathbf{A} , \mathbf{b} , \mathbf{C}_v is a nonlinear problem solved by means of an iterative approach, an initial reliable solution close to the optimum is provided. We start by putting $\mathbf{a} = [1, \dots, 1]^T$ and $\mathbf{A} = A_{id}(f)$ for all the images, then iteratively solve, in sequence, $b_{m,p}$, $\sigma_{m,p}^2$, $A_{m,n}$ and finally the gains a_n , until a stop criterion is reached.

ACKNOWLEDGMENT

The authors would like to thank A. S. Italiana for providing the Cosmo SkyMed Datasets.

REFERENCES

- [1] C. Prati, A. Ferretti, and F. Rocca, "Permanent scatterers in SAR interferometry," *IEEE Trans. Geosci. Remote Sens.*, vol. 39, no. 1, pp. 8–20, Jan. 2001.
- [2] D. Perissin and A. Ferretti, "Urban-target recognition by means of repeated spaceborne SAR image," *IEEE Trans. Geosci. Remote Sens.*, vol. 45, no. 12, pp. 4043–4058, Dec. 2007.
- [3] G. Fornaro, A. Monti Guarnieri, A. Pauciuolo, and S. Tebaldini, "Joint multi-baseline SAR interferometry," *EURASIP J. Appl. Signal Process.*, vol. 20, pp. 3194–3205, Dec. 2005.
- [4] G. Fornaro, A. Pauciuolo, and F. Serafino, "Deformation monitoring over large areas with multipass differential SAR interferometry: A new approach based on the use of spatial differences," *Int. J. Remote Sens.*, vol. 30, pp. 1455–1478, Apr. 2009.
- [5] A. Ferretti, C. Prati, and F. Rocca, "Nonlinear subsidence rate estimation using the permanent scatterers in differential SAR interferometry," *IEEE Trans. Geosci. Remote Sens.*, vol. 38, no. 5, pp. 2202–2212, Sep. 2000.
- [6] C. Colesanti, A. Ferretti, C. Prati, D. Perissin, and F. Rocca, "ERS-ENVISAT permanent scatterers interferometry," in *Proc. IEEE Int. Geosci. Remote Sens. Symp.*, Jul. 2003, pp. 1130–1132.
- [7] D. D'Aria, A. Ferretti, A. Monti Guarnieri, and S. Tebaldini, "SAR calibration aided by permanent scatterer," *IEEE Trans. Geosci. Remote Sens.*, vol. 48, no. 4, pp. 2076–2086, Apr. 2010.
- [8] P. Guccione, A. Monti Guarnieri, and S. Tebaldini, "Stable target detection and coherence estimation in interferometric SAR stacks," *IEEE Trans. Geosci. Remote Sens.*, vol. 50, no. 8, pp. 3171–3178, Aug. 2012.
- [9] F. Tupin, H. Maitre, C. Tison, J. M. Nicolas, "A new statistical model for Markovian classification of urban areas in high resolution SAR images," *IEEE Trans. Geosci. Remote Sens.*, vol. 42, no. 10, pp. 2046–2057, Oct. 2004.
- [10] A. Monti Guarnieri and P. Guccione, "ML antenna pattern shape and pointing estimation in synthetic aperture radar," in *Proc. 31st EARSel Symp.*, 2011, pp. 487–498.
- [11] A. Monti Guarnieri and P. Guccione, "Maximum likelihood estimation of SAR azimuth antenna by means of persistent point scatterers," in *Proc. IEEE Int. Geosci. Remote Sens. Symp.*, Jul. 2012, pp. 5494–5497.
- [12] F. Rocca, C. Prati, and A. Monti Guarnieri, "Spot mode SAR focusing with the W–K technique," in *Proc. Geosci. Remote Sens. Symp.*, Jun. 1991, pp. 631–634.
- [13] R. M. Majeowski, W. G. Carrara, and R. S. Goodman, *Spotlight Synthetic Aperture Radar*. Norwood, MA, USA: Artech House, 1995.
- [14] P. Hartl and R. Bamler, "Synthetic aperture radar interferometry," *Inverse Problems*, vol. 14, no. 4, pp. R1–R54, 1998.
- [15] S. Serpico, G. Moser, and J. Zerubia, "SAR amplitude probability density function estimation based on a generalized gaussian model," *IEEE Trans. Image Process.*, vol. 15, no. 6, pp. 1429–1442, Jun. 2006.
- [16] J. Zerubia, S. Serpico, V. A. Krylov, and G. Moser, "Enhanced dictionary-based SAR amplitude distribution estimation and its validation with very high-resolution data," *IEEE Geosci. Remote Sens. Lett.*, vol. 8, no. 1, pp. 148–152, Jan. 2011.
- [17] G. Schreier, *SAR Geocoding: Data and Systems*, Karlsruhe, Germany: Wichmann, 1990.
- [18] A. Monti Guarnieri and P. Guccione, "Accurate optimal doppler centroid estimation for SAR data," in *Proc. Geosci. Remote Sens. Symp.*, Jul. 2011, pp. 2460–2463.
- [19] S. Tam, H. Jackson, and I. Sinclair, "ENVISAT ASAR precision transponder," in *Proc. CEOS SAR Workshop*, 1999, pp. 311–316.
- [20] D. Giudici and A. Monti Guarnieri, "Accurate estimate of the azimuth antenna pattern from SAR images," in *Proc. 6th Eur. Conf. Synth. Aperture Radar*, 2006, pp. 1–4.
- [21] I. G. Cumming, "A spatially selective approach to doppler estimation for frame-based satellite SAR processing," *IEEE Trans. Geosci. Remote Sens.*, vol. 42, no. 6, pp. 1135–1148, Jun. 2004.
- [22] S. N. Madsen, "Estimating the doppler centroid of SAR data," *IEEE Trans. Aerosp. Electron. Syst.*, vol. 25, no. 2, pp. 135–140, Mar. 1989.
- [23] C. Cafforio, P. Guccione, and A. Monti Guarnieri, "Doppler centroid estimation for ScanSAR data," *IEEE Trans. Geosci. Remote Sens.*, vol. 42, no. 1, pp. 14–23, Jan. 2004.
- [24] S. Tebaldini, P. Guccione, and A. Monti Guarnieri, "Automatic quality assessment for interferogram SAR stacks," in *Proc. Geosci. Remote Sens. Symp.*, Jul. 2011, pp. 1345–1348.
- [25] A. Tarantola, *Inverse Problem Theory*. Amsterdam, The Netherlands: Elsevier, 1994.
- [26] R. Vigiotti, G. Manoni, F. Caltagirone, and P. Spera, "SkyMed/COSMO mission overview," in *Proc. IEEE Int. Geosci. Remote Sens. Symp.*, Jul. 1998, pp. 683–685.